JOURNAL OF OPTOELECTRONICS AND ADVANCED MATERIALS Vol. 12, No. 10, October 2010, p. 2044 - 2051

Optical characterization of biological tissues using nanoscale FinFET photodetector

R. RAMESH*, M. MADHESWARAN[a], K. KANNAN[b]
Department of Electronics and Communication Engineering, M.A.M College of Engineering, Trichy – 621 105, TamilNadu, India
[a]*Center for Advanced Research, Muthayammal Engineering College, Rasipuram-637 408, TamilNadu, India*
[b]*Department of Mathematics, SASTRA University, Thanjavur, TamilNadu, India*

A non-invasive optical method for the characterization of biological tissues using nanoscale FinFET photodetector by wavelet approach has been theoretically developed and presented in this paper. To the best of our knowledge, this approach is the first of its kind for classifying the skin tissue and muscle tissue by determining the surface potential variations of nanoscale FinFET photodetector illuminated by a laser source. The compositional variation of various tissues could be determined by solving the 3-D Poisson-Schrödinger equation using interpolating wavelets. The optical parameters such as absorption and reduced scattering coefficients are also estimated. By this method, the point-to-point variation in tissue composition and structural variation in healthy and diseased tissues could be determined. The results obtained are used to examine the performance of the device for its suitable use as a nanoscale sensor for classification of different tissues.

(Received September 5, 2010; accepted October 14, 2010)

Keywords: FinFET photodetector, Biological Tissue, Optical characterization

1. Introduction

The non-invasive methods for monitoring and diagnosis of pathological changes in tissues are of great importance in medical diagnostics and therapeutics. Ionizing radiation such as X-ray may be used for the diagnosis of skeletal abnormalities. Soft tissue lesions and coronary blood vessels may be diagnosed using angiography. Breast cancers can be detected using mammography and reconstruction of tomographic images, etc. Due to the ionizing radiation of these methods, continuous or frequent monitoring is not recommended. Magnetic Resonance Imaging (MRI) and positron emission tomography methods are expensive and require contrast agents, for which many people are allergic. Optical techniques due to their nonionic, noninvasive, inexpensive characteristics emerge as an alternative diagnostic technique [1]. Laser radiation characterizes by nearly single frequency, high degree of temporal and spatial coherence, high intensity and plane polarized. When a laser beam is incident on a thick tissue surface, due to mismatch in the refractive index at the air-tissue interface, a part of the laser light is back scattered, whereas the remaining part is absorbed in the tissues [2]. The spatial distribution of backscattered and transmitted components of the laser contains information about the structure, metabolic and physiologic activities of tissues [3]. Optical reflectance imaging of tissues is applied to determine the variation in the internal structure of tissues. The absorption and scattering variation in biological tissues is influenced by the absorption (μ_a) and reduced scattering (μ'_s) coefficients representing the attenuation of incident radiation and scattering per incremental unit photon path length in a tissue [4]. These parameters for intact organs can be determined by the experimental measurement of the spatial variation of the reflectance on the tissue surface and matching of this curve by iterative procedure or Monte Carlo procedure. R.Srinivasan et al., have determined the variability of optical parameters at various regions of the human forearm using Monte Carlo simulation and their images are reconstructed [5]. The transmitted component, after passing through the thinner, complex tissues (finger) and thicker, soft tissues (breast, testis etc.) also contains information on selective absorption by the internal tissue components [6]. Due to the recent development of fast detecting systems using short pulses, it is possible to detect the partially coherent photons and suppress excessively scattered photons [7]. Human body consists of layered structures of different tissues having distinct optical properties. It has been shown experimentally and theoretically that the diffused reflectance components scattered from the upper and deeper layers of tissues appear closer or further from the beam entry point [8,9]. After undergoing various processes in the tissue, the backscattered photons over the surface help in the analysis and reconstruction of images of the internal structure. A neural network based approach for determination of optical properties of biological properties has been reported [10].

The photosensitivity and the integrated circuit compatibility of Field-Effect Transistors (FETs) have extended potential of these devices for their use as photodetectors. Among the FETs configuration, Metal Semiconductor Field Effect Transistor (MESFET) and High Electron Mobility Transistor (HEMT) have been studied theoretically as well as experimentally by several works for various optically-controlled applications [11]. A three dimensional modeling of a nano MISFET photodetector without including quantum mechanical effects [12] has been reported. A transition from bulk to multiple-gate fully depleted (FD) silicon-on-insulator (SOI) offers drive current and better short-channel immunity [13]. Complementary Metal oxide Semiconductor (CMOS) designs below 0.1µm are severely constrained by short channel effects (SCE) and gate insulator tunneling [14]. One of the approaches to circumvent the gate tunneling restriction is to change the device structure so that the MOSFET gate length can be further scaled even with thicker oxide. Double-gate MOSFET (DGFET) is one of the most promising devices for channel length in the range 10-30 nm [15].In order to optimize the performance of double gate devices, self-aligned processes and structures are proposed, with FinFET being one of the most promising [16]. The potential variation in the channel used to calculate the subthreshold current and threshold voltage of FinFETs with doped and undoped channels has been reported [17]. An analytical model based on 3-D analysis for an undoped channel has been reported [18].El Hamid et al., [19] presented the 3-D analytical modeling including mobile charge term. W. Yang et al., [20] reported the scaling theory of FinFET by 3-D analytical solution of Poisson’s equation in channel region. The existing literatures reported on analytical modeling have shown the complexity in evaluating various device characteristics including quantum mechanical effects. In addition, it has been found that many assumptions and approximations have to be incorporated while the device is analytically modeled. Quantum mechanical modeling is important for many reasons, e.g., the tunneling current through ultra-thin gate oxide adds to the low limit of the off-state current [21].In FinFET devices, quantum effects and non-equilibrium, ballistic or near-ballistic transport has large impact on device performance [21].In recent years, the problem of partial differential equation (PDE) solution has also been solved by means of new mathematical tools, such as the wavelet theory [22]. But they have found solution for 2D simulation without including quantum mechanical effects. Wavelet coefficients have been used in time-varying problems as the parameter that controls the accuracy of the solution [23], but this approach computes the solution on a uniform grid at the finest resolution [24]. On the other hand, implementing a technique that adaptively refines the mesh in domains where the unknown quantities vary rapidly would considerably reduce the number of unknowns. Such a technique corresponds to a multiresolution analysis (MRA) of a problem. A very attractive way of implementing a multiresolution analysis is to use wavelets. It was demonstrated [25] that finite-difference scheme can be derived with wavelet expansions. The resulting numerical technique is called multiresolution time-domain technique (MRTD) [26].This method shows very good performance as for the accuracy, memory requirements and CPU time. The MRTD can be regarded as a wavelet-based Galerkin method. For nonlinear equations used for semiconductor device modeling, this method can become quite time consuming. M. Toupikov et. al., proposed a nonlinear modeling of semiconductor devices by solving 2D Poisson’s equation using sparse point representation based on interpolating wavelets [27]. A WKB interpolation-Wavelet method for 3-D numerical simulation of nanoscale FinFET photodetector has been proposed [28].

In this paper, the optical properties of the biological tissues are theoretically estimated by determining the surface potential variations of nanoscale FinFET using interpolating wavelet approach. The variation in the characteristics of nanoscale FinFET are calculated by solving the 3D Poisson- Schrödinger equations numerically until self-consistency is achieved. The interpolating wavelet method produces more accurate results with much coarser grids and the optical parameters of skin and muscle tissues are estimated by ignoring the background dark noise of the nanoscale FinFET.

2. Physics based modeling

The general FinFETs structure is shown in Fig.1. The geometrical parameters and the boundary conditions are given as [20]

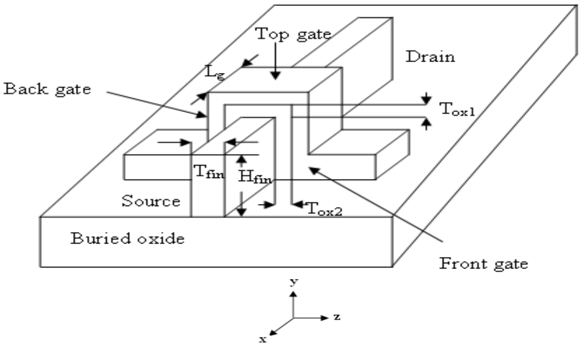

Fig. 1. Schematic diagram of FinFET.

i) Gate Length (L_g): The physical gate length of FinFETs, defined by spacer gap.

ii) Fin Height (H_{fin}): The height of silicon fin, defined by the distance between the top gate and buried oxide layer (BOX).

iii) Fin Width (T_{fin}): The thickness of silicon fin, defined between the front and back gates.

iv) Top gate thickness (T_{ox1}): The thickness of the top gate oxide.

v) Front or back gate thickness (T_{ox2}): The thickness of the front or back gate oxide.

vi) Channel Length (L_{eff}): The channel length is estimated by the metallurgical junction for abrupt junctions.

Geometrical channel width defined as W=2x H_{fin} + $T_{fin.}$

The boundary conditions are

$$U\Big|_{y=H_{eff}} = V_g - V_{fb}.$$

$$U\Big|_{z=-T_{eff}/2} = V_g - V_{fb}.$$

$$U\Big|_{z=T_{eff}/2} = V_g - V_{fb}.$$

$$U\Big|_{x=0} = V_{bi}$$

$$U\Big|_{x=L_{eff}} = V_{bi} + V_{ds}$$

$$U\Big|_{y=-H_{eff}} = V_g - V_{fb}.$$

The electrostatic potential in the subthreshold region of nanoscale FinFET under illumination from tissue surface can be described by the 3-D Poisson's equation.

$$\frac{\partial^2 U(x,y,z)}{\partial x^2} + \frac{\partial^2 U(x,y,z)}{\partial y^2} + \frac{\partial^2 U(x,y,z)}{\partial z^2} = \frac{q[N_a(x,y,z) - n(x,y,z) + p(x,y,z)]}{\varepsilon_s} + \Delta n - \Delta Q \tag{1}$$

where $U(x,y,z)$ is the surface potential at a particular point (x,y,z), $N_a(x,y,z)$ is the uniform channel doping concentration, q is the electronic charge, ε_s is the permittivity of silicon, $n(x,y,z)$ is the electron concentration, $p(x,y,z)$ is the hole concentration, Δn is the excess carriers generated per unit volume, ΔQ is the attenuated intensity.

$$n(x,y,z) = \sum_{j=1}^{3} \sum_{i=1}^{\infty} n_{ij} \left|\psi(x,y,z)\right|^2 \tag{2}$$

where j is the valley and i is the subband.

$$n_{ij} = \frac{n_{vj} m_{dj} k_B T}{\pi \hbar^2} \ln\left[1 + \exp\left(\frac{E_{Fn} - E_{ij}}{k_B T}\right)\right] \tag{3}$$

where (3) expresses the number of electrons occupying the ij th electron energy level, m_{dj} is the electron density-of-states mass, n_{vj} is the valley degeneracy, E_{fn} is the electron quasi-Fermi level, E_{ij} is the electron energy states.

The excess carriers generated per unit volume due to the absorption of incident optical power density are given by [6]

$$\Delta n = \frac{1}{W_m} \int_0^{W_m} G_{op}(x) \tau_L \, dy \tag{4}$$

where W_m is the maximum width of the depletion layer and is given by

$$W_m = [4\varepsilon_s \ln(N_a / n_i) / q\beta N_a]^{1/2} \tag{5}$$

where N_a is the acceptor concentration. $G_{op}(x)$ is the excess carrier generation rate at any point x in the semiconductor and is given by

$$G_{op}(x) = \frac{p_{opt}}{h\gamma}(1 - R_m)(1 - R_i)(1 - R_s)\alpha e^{-\alpha y} \tag{6}$$

where P_{opt} is the incident optical power density, h is the Planck's constant, γ is the operating frequency, α is the absorption coefficient of the semiconductor at the operating wavelength, R_m, R_i, R_s are the reflection coefficient at the metal gate entrance, gate-insulator interface and the insulator-semiconductor interface.

To determine the optical parameters at each point on the body surface, the following assumptions are made [9].

(i) the photons incident upon the tissue were considered as neutral particles.

(ii) the tissue was considered to be a homogenous medium.

(iii) the beam of photons was considered to be monochromatic.

The incident photon beam profile with each photon of unit intensity (WT_1) is considered. Fig.2. shows the simulated propagation path of a photon incident on the tissue surface. The simulation process is initiated by launching a light beam, which splits into many photon packets, with initial weight WT_1 and allowed to pass through the biological medium in a given direction. After traveling a distance L in the biological medium, the photon packet is assumed to interact with the medium and a fraction WT_2 of this packet is deposited at the point of interaction after wards a new direction of the photon packet is simulated.

Due to skin tissue-photon interaction, the attenuated intensity considering the refractive index of two media is given by

$$\Delta Q = (WT_1)\left(\mu_a \big/ \mu_t\right) \times \left(\frac{n_2}{n_1}\right) \tag{7}$$

μ_a is the absorption coefficient (cm^{-1}), n_1 is the refractive index of first medium and n_2 is the refractive index of second medium. The total attenuation coefficient is given by

$$\mu_t = \left(\mu_s' + \mu_a\right) \tag{8}$$

The reduced scattering coefficient is calculated from

$$\mu_s' = \mu_s(1 - g) \tag{9}$$

The scattering coefficient μ_s and the anisotropy parameter g are combined in the reduced scattering coefficient μ_s'

In the wavelength band of 600-1300nm, the absorption coefficient μ_a is approximately 0.1-10cm^{-1} and the scattering coefficient μ_s is 100-1000cm^{-1} for soft tissues. Typical values of the anisotropy parameter g are between 0.8 and 0.95 for all tissues. The reported values of refractive index for soft tissues are between 1.38 and 1.41 for 630nm [29]. The effective attenuation coefficient $\mu_{eff} = \sqrt{3\mu_a \mu_t}$ and the total attenuation coefficient μ_t are the two optical parameters that are used to calculate the reflectance of the tissues. The analytic expression for the reflectance is given by

$$R(\rho)=\frac{a'}{4\pi}\left[\frac{1}{\mu_t}\left(\mu_{eff}+\frac{1}{r_1}\right)\frac{\exp(-\mu_{eff}r_1)}{r_1^2}\right]+\left(\frac{1}{\mu_t}+2z_b\right)\left(\mu_{eff}+\frac{1}{r_2}\right)\left(\frac{\exp(-\mu_{eff}r_2)}{r_2^2}\right) \quad (10)$$

$$r_1=\left[\left(\frac{1}{\mu_t}\right)^2+\rho^2\right]^{1/2}, r_2=\left[\left(\frac{1}{\mu_t}+2z_b\right)^2+\rho^2\right]^{1/2}$$

and

$$a' = \mu_s' \big/ (\mu_a + \mu_s')$$

The path length l in the tissue medium considering the refractive index is given by

$$l = -(\ln R)/\mu_t \times \left(\frac{n_2}{n_1}\right)$$

where R is a random number between 0 and 1.

After passing through a certain distance in the muscle tissue medium, the new photon intensity (WT_2) coming out from the muscle tissue is calculated by

$$WT_2 = WT_1(\mu_s'/\mu_t)\times\left(\frac{n_2}{n_1}\right) \quad (11)$$

After position 2, the photon is scattered and deflected. The deflection angle θ is calculated by

$$\cos\theta = \frac{1}{2g}\left[1+g^2-\left\{\frac{(1-g^2)}{(1-g+2g\varsigma)}\right\}^2\right] \text{for } g \neq 0 \quad (12)$$

ς is random number between 0 and 1.

If scattering is isotropic (g=0), the instantaneous value of $\cos\theta$ is calculated from
$\cos\theta = (2\varsigma - 1)$

The azimuthal angle ϕ is given by

$$\phi = 2\pi\gamma$$

where γ is a random number between 0 and 1. Once the deflection angle and azimuthal angle are chosen, the new direction of photon packet can be calculated.

A photon is described by three spatial coordinates for the position and two directional angles for the direction. However, it is convenient to describe the spatial position with three Cartesian coordinates and the direction of travel with three direction cosines. The direction cosines are obtained by taking the cosine of the angle that the photon's direction makes with each axis. These are specified by μ_x, μ_y and μ_z corresponding to x, y, z axes respectively.

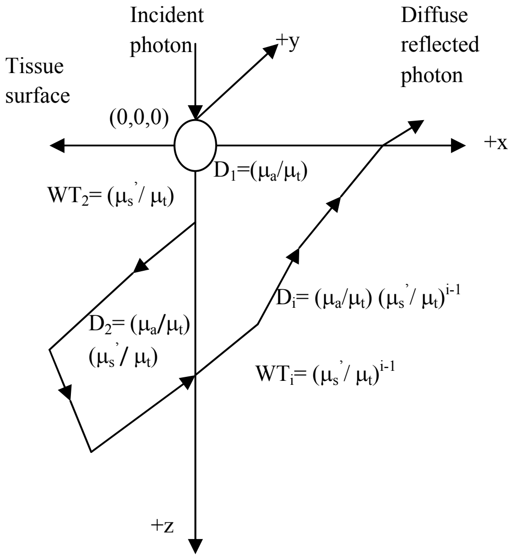

Fig. 2. Schematic diagram of photon path in the tissue.

For a photon located at (x,y,z) traveling a distance ΔS in the direction (μ_x,μ_y,μ_z), the new coordinates are given by (x',y',z')

$$x' = x + \mu_x \Delta S, \quad y' = y + \mu_y \Delta S, \quad z' = z + \mu_z \Delta S$$

$$\mu_x' = \frac{\sin\theta}{\sqrt{1-\mu_z^2}}(\mu_x\mu_z\cos\phi - \mu_y\sin\phi) + \mu_x\cos\theta \quad (13)$$

$$\mu_y' = \frac{\sin\theta}{\sqrt{1-\mu_z^2}}(\mu_y\mu_z\cos\phi + \mu_x\sin\phi) + \mu_y\cos\theta \quad (14)$$

$$\mu_z' = -\sin\theta\cos\phi\sqrt{1-\mu_z^2} + \mu_z\cos\theta \quad (15)$$

If the angle of the photon packet is too close to normal of the tissue surface $(|\mu_z| > 0.99999)$, the following formulas are used to obtain new photon directions.
$\mu_x' = \sin\theta\cos\phi$, $\mu_y' = \sin\theta\sin\phi$, $\mu_z' = SIGN(\mu_z)\cos\theta$
$SIGN(\mu_z)$ returns 1 when μ_z is positive and it returns -1 when μ_z is negative.

3. Multiresolution analysis and wavelets

Multiresolution Analysis (MRA) is an important concept in wavelet theory. Many useful orthonormal wavelets are constructed within this framework. The usefulness of wavelets for solving partial differential equations relies on the definition of MRA. An MRA is based on two fundamental concepts: nested subspaces and orthonormal bases. The first decomposes the information into different scales; the second allows stable and fast algorithms. The space of square integral functions on the real line is denoted by $L^2(R)$.The orthonormal basis of wavelets of $L^2(R)$ is formed by dilations and translations of a single function $\Psi(x)$, called a mother wavelet. The interpolating wavelet method provides more accurate results than other methods.

$$\Psi_{jk}(x) = 2^{j/2}\Psi(2^j x - k),\ j,k \in \mathrm{Z}. \tag{16}$$

The function $\Psi(x)$ has a companion, the scaling function $\varphi(x)$.They both satisfy the following two-scale relation

$$\varphi(x) = \sum_k a_k \varphi(2x - k), \tag{17}$$

$$\Psi(x) = \sum_k (-1)^k a_{1-k}\varphi(2x - k), \tag{18}$$

where the coefficients $a_k (k = 0,1,...L-1)$ appearing in the two-scale relations (17) and (18) are called the wavelet filter coefficients. The support of the scaling function φ is the interval $[0, L-1]$ while that of the corresponding wavelet Ψ is the interval $[1-L/2, L/2]$. The Daubechies wavelet filter coefficients for $L = 4,6,8,10$ are listed in [23].

The 3D effective mass Schrödinger equation along the n-channel is given by [21]

$$-\left[\frac{\hbar^2}{2m_x^*}\frac{\partial^2}{\partial x^2} + \frac{\hbar^2}{2m_y^*}\frac{\partial^2}{\partial y^2} + \frac{\hbar^2}{2m_z^*}\frac{\partial^2}{\partial z^2} + qU_{(x,y,z)}\right]\psi_{x,y,z} = E\psi_{x,y,z} \tag{19}$$

In the above equation m_x^*, m_y^*, m_z^* are effective masses in the x, y and z directions. $m_x^* = m_l = 0.916m_0, m_y^* = m_t = 0.19m_0, m_z^* = m_t = 0.19m_0$. E is the eigen energy, ħ is the reduced Planck's constant, q is the charge of an electron U(x, y, z) is the surface potential, ψ(x, y, z) is the eigen wave function. The mixed Dirichlet and von Neumann boundary conditions were used for solving the 3-D Schrödinger equation because the Dirichlet boundary conditions force density of electrons to decrease to zero at contacts while density increases under von Neumann boundary conditions. For these reasons, the 3-D Schrödinger equation is solved using Dirichlet and von Neumann boundary conditions and normalized the states to 1/2. The mixed Dirichlet and von Neumann boundary conditions are given by

$$\int |\psi_n(z)|^2 dz = 1/2 \tag{20}$$

This means that a constant function is obtained by summing the cosine functions from Dirichlet boundary conditions and the sine functions from von Neumann boundary conditions with normalization to 1/2.By solving the Schrödinger equation, the quantized states that are occupied by local quasi-Fermi levels were obtained.

In this section, the direct solution of 3-D Schrödinger equation (19) with mixed Dirichlet and Von Neumann boundary conditions is obtained using Wavelet method. The Wavelet approximation to the solution $\psi_j(x,y,z)$ at scale j is

$$\psi_j(x,y,z) = \sum_k\sum_l\sum_m \tilde{c}_{k,l,m} 2^{j/2}\varphi(2^j x - k) 2^{j/2}\varphi(2^j y - l) 2^{j/2}\varphi(2^j z - m)$$
$$k,l,m \in Z \tag{21}$$

where $\tilde{c}_{k,l,m}$are the wavelet coefficients. (i.e.) they define the solution in wavelet space.

Equation (21) can be simplified into

$$\sum_k\sum_l\sum_m \tilde{c}_{k,l,m}\varphi_{jk}(x)\varphi_{jl}(y)\varphi_{jm}(z) \tag{22}$$

where

$$\varphi_{jk}(x)=2^{j/2}\varphi_{jk}(2^j x-k),\varphi_{jl}(y)=2^{j/2}\varphi_{jl}(2^j y-l),\varphi_{jm}(z)=2^{j/2}\varphi_{jm}(2^j z-m),$$
$$j > 0,$$

$k,l,m = 2-N, 3-N, ...,2^j - 1$ are $2^j + N - 2$ unknown coefficients. j fixes the level of resolution. The larger the value of j, the more accurate a solution can be obtained. But the number of equations required to solve the unknown coefficients is increased. In equation (22), the parameter N represents that the wavelet associated with the set of N Daubechies filter coefficients is used as the solution bases. Substituting the wavelet series approximation $\psi_j(x,y,z)$ in equation (22) for $\psi(x,y,z)$ yields

$$\sum_k\sum_l\sum_m \tilde{c}_{k,l,m}\begin{pmatrix} -\frac{\hbar}{2m_x^*}\frac{d^2}{dx^2}\phi_{jk}(x) - \frac{\hbar}{2m_y^*}\frac{d^2}{dy^2}\phi_{jk}(y) - \frac{\hbar}{2m_z^*}\frac{d^2}{dz^2}\phi_{jk}(z) + \\ (qU_{x,y,z} - E)\phi_{jk}(x)\phi_{jl}(y)\phi_{jm}(z) = 0 \end{pmatrix} \tag{23}$$

To determine the coefficient $c_{k,l,m}$, we take the inner product of both sides of equation (23) with φ_{jn}

$$\sum_k\sum_l\sum_m \tilde{c}_{k,l,m}\left(-\frac{\hbar^2}{2m_x^*}\right)\int_0^{L_{eff}} \phi''_{jk}(x)\phi_{jn}(x) - \frac{\hbar^2}{2m_y^*}\int_0^{H_{eff}} \phi''_{jl}(y)\phi_{jn}(y) - \frac{\hbar^2}{2m_z^*}\int_0^{T_{eff}} \phi''_{jm}(z)\phi_{jn}(z) +$$

$$(qU_{x,y,z} - E)\phi_{jk}(x)\phi_{jl}(y)\phi_{jm}(z) = 0$$

For

$$n = 2 - N, 3 - N, \ldots 2^{j} - 1 \tag{24}$$

where prime ', denotes differentiation with respect to the indicated independent variable, L_{eff} is the length of the channel , H_{eff} is the height of the fin, T_{eff} is the thickness of the fin. The above equation is solved using Cholesky's decomposition method

4. Computational technique

The 3D Poisson's equation (1) with the boundary conditions under illumination from skin and muscle tissues are solved numerically using Leibmann's iteration method to determine the approximate surface potential for a fixed value of gate voltage and assumed value of drain voltage. This value of surface potential is given to the 3D Schrödinger equation (19). The 3-D Schrödinger equation is solved directly using the Dirichlet and von Neumann boundary conditions by interpolating wavelet method and the exact value of surface potential is obtained for the skin and muscle tissues. The absorption and scattering coefficients are estimated using the surface potential values of the nanoscale FinFET.

5. Results and discussion

Numerical computation has been carried out for the nanoscale FinFET. The parameters used for the calculation are given in Table 1.

Table. 1. Parameters and constants.

Parameter	Value
Gate Length (L_g)	30 nm
Top gate oxide thickness (T_{ox1})	5 nm
Front (or) back gate thickness (T_{ox2})	1 nm
Channel Length (L_{eff})	30 nm
Thermal Voltage (V_T)	0.025852 V
Intrinsic carrier concentration (n_i)	$9.65 \times 10^9/cm^3$
Acceptor concentration (N_a)	$1 \times 10^{16}/cm^3$
Flatband voltage (V_{fb})	-0.48 V
Built-in potential (V_{bi})	0.6 V
Gate voltage (V_g)	0.2V
Wavelength of light source (λ)	630nm
Refractive index of skin (n_1), muscle (n_2)	1.38,1.41

Fig. 3 shows the potential profile of the FinFET photodetector under normal illumination using interpolating Wavelet method on a grid of 20 x 13 x 10 points. The surface potential $U(x,y,z)$ is calculated for different values of x and constant values of y and z, ignoring the background dark noise of the device. The figure also shows the illumination results from skin and muscle tissues using the same wavelet method. The surface potential values under illuminated conditions are calculated for P_{opt}=0.5W/m^2 and V_{DS}=1.5V. It is also found that the surface potential values decreases than the normal illumination when the FinFET is illuminated by the source of light that arrives from the skin and muscle tissues. The decrease of illumination is more pronounced in the muscle tissue. This is due to the fact that excess carriers generated due to illumination from skin and muscle tissues are very much less than the carriers generated under normal illumination condition and this decreases the conductivity of the channel.

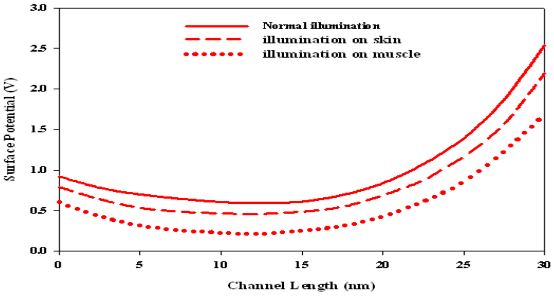

Fig. 3. Surface potential calculation along channel length for skin and muscle tissue for P_{opt}=0.5W/m^2 and V_{ds}=1.5V.

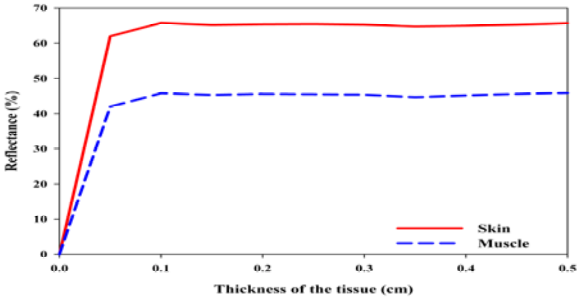

Fig. 4. Variation of reflectance for skin and muscle tissue.

Fig. 4 shows the variation in reflectance with the increase in thickness of the tissue. Initially, this optical parameter increases with increase in thickness of the tissue and attains its maximum value as it reaches the depth of the tissue. This constant value is due to the self absorption of photons within the thickness of the tissue, thus minimizing the influence of tissue reflectance. It is found that the reflectance is higher for the muscle tissue than the skin tissue.

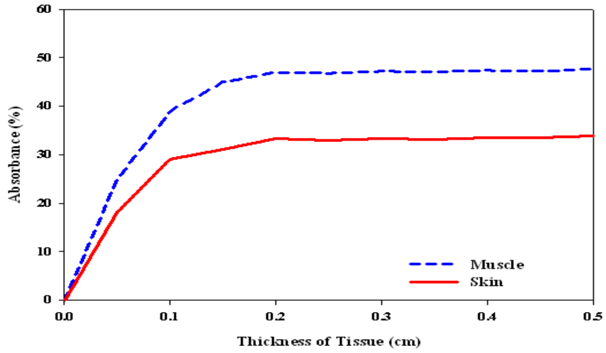

Fig. 5. Variation of absorption for skin and muscle tissue.

Fig. 5 shows the variation of absorption of illumination in the skin and muscle tissue. It is also found that the absorption is more pronounced in muscle tissue than the skin tissue. This is due to the fact that the excess carriers generated under illumination are absorbed by the different layers of muscle tissue than the skin tissue.

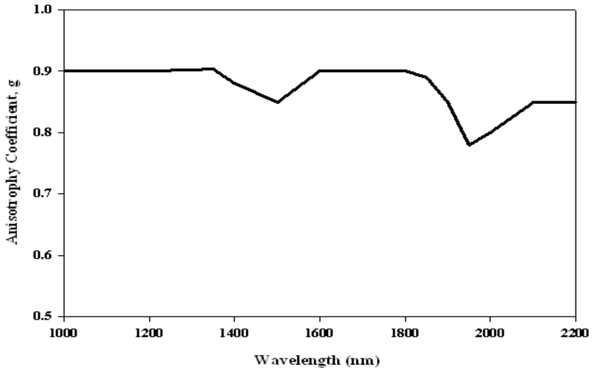

Fig. 6. Anisotrophy coefficient in muscle tissue as a function of wavelength.

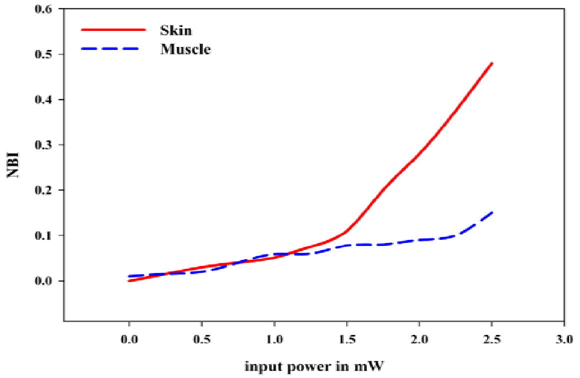

Fig. 7. NBI variation for skin tissue and muscle tissue for different input power.

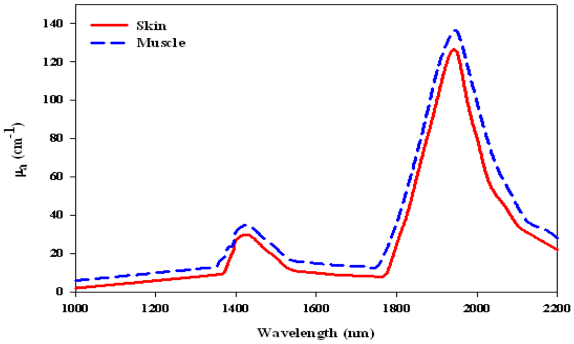

Fig. 8. Absorption coefficient as a function of wavelength in skin and muscle tissue.

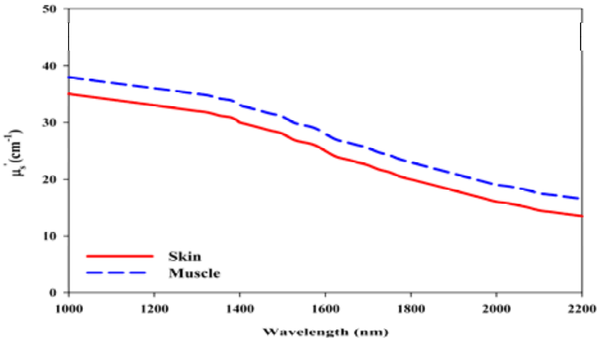

Fig. 9. Scattering coefficient as a function of wavelength in skin and muscle tissue.

Fig. 6 shows the estimated values of anisotropy coefficient as a function of wavelength. It is found that the anisotropy coefficient varies between 0.8 and 0.9. This is due to the fact that the light is forward scattered in tissues. The normalized backscattered intensity (NBI) as a function of input power is shown in Fig. 7 for skin and muscle tissue. The NBI profile increases with an increase in input power. It is also found that the NBI is more for skin tissue than the muscle tissue. Fig. 8 shows the absorption coefficient of skin and muscle tissues. It is found that a high degree of absorption in the wavelength between 1900-2050 nm due to matching of energy in the bandgap structure of the molecules in chromophores and the energy of the incident radiation between those wavelengths. This causes losing of energy and produces high peaks of absorption coefficient. The increase of absorption in muscle tissue than the skin tissue is due to the presence of more than one type of tissue in muscle tissue. Fig. 9 shows the scattering coefficient variation of skin and muscle tissue as a function of wavelength. It is found that the scattering coefficient decreases as the wavelength increases. It is also found that due to the presence of several layers in muscle tissue, the scattering is more pronounced than the skin tissue.

6. Conclusions

The wavelet based approach for optical characterization of biological tissues using nanoscale FinFET shows that the FinFET photodetector may retain performance acceptable for biomedical applications. The present work is confined to the characterization of only the skin and muscle tissues and their optical parameters are estimated using the surface potential variations of the nanoscale FinFET. In the future work, the same characteristics of nanoscale FinFET may be used to characterize tumor and phantom cells and their optical parameters can be estimated. Neural networks and optimization techniques can also be implemented to extract the needed optical parameters.

References

[1] R. Srinivasan, D. Kumar, Megha Singh, Current Science **87**, 218 (2004).

[2] B. C. Wilson, S. L. Jaques, IEEE J. Quantum Electron. **26**, 2186 (1990).

[3] W. Cui, L. E. Ostrander, IEEE Trans. Biomed. Eng. **39**, 194 (1992).

[4] M. Singh, S. Chako, Current Science **43**, 1015 (1997).

[5] T. J. Farrel, B. C. Wilson, M. S. Patterson, Phys. Med. Biol. **37**, 2281 (1992).

[6] R. Srinivasan, M. Singh, IEEE Trans. Biomed. Eng. **50**, 724 (2003).

[7] G. Mitic, J. Olzer, J. Otto, P. Erich, G. Solkner, W. Zenith, Appl. Opt. **33**, 6699 (1994).

[8] S. Chacko, M. Singh, Med. Biol. Eng. Comput. **37**, 278 (1999).

[9] D. Kumar, S. Chacko, M. Singh, Indian J. Biochem. Biophys. **36**, 330 (1999).

[10] D. Warncke, E. Lewis, S. Lochmann, M. Leahy, Journal of physics, Conference series **178**, 012047 (2009).

[11] P. Chakrabarti, S. Kumar, P. Rout, B. G. Rappai, Proceeding3rd Asia Pacific Microwave Conference, Tokyo, Japan 575 (1990).

[12] M. Kabeer, K. Gowri, V. Rajamani, J. Optoelectron. Adv. Mater. **9**(9), 2879 (2007).

[13] J.-P.Colinge, Solid state Electron. **48**(6), 897 (2004).

[14] Y. Taur, L. H. Wann, D. J. Frank, in IEDM Tech. Dig., 789 (1998).

[15] D. J. Frank, S. E. Laux, M. V. Fischetti, in IEDM Tech. Dig., 553 (1992).

[16] H.-S. P. Wong, K. K. Chan, Y. Taur, in IEDM Tech. Dig., 427 (1997).

[17] S. D. Havaldar, G. Katti, N. DasGupta, A. DasGupta, IEEE Trans.Electron Devices **53**(4), 737 (2006).

[18] G. Pei, J. Kedzierski, P. Oldiges, M. Ieong,V. Chin-Chaun Kan , IEEE Trans.Electron Devices **49**(8), 1411 (2002).

[19] H. A. El Hamid, J. R. Guitart, V. Kilchytska, D. Flandre, B. Iniguez, IEEE Trans. ElectronDevices **54**(9), 2487 (2007).

[20] W. Yang, Z. Yu, L. Tian, IEEE Trans. Electron Devices **54**(5), 1140 (2007).

[21] X. Shao, Z. Yu, Solid-State Electronics **49**, 1435 (2005).

[22] L. De Marchi, F. Franze, E. Baravelli, Solid-stateElectronics **50**, 650 (2006).

[23] L. Jameson, SIAM J. SCI Comput. **19**, 1980 (1998).

[24] I. Fatkulin, J. S. Hesthaven, Scientific computing report series, 2001.

[25] M. Krumholz, L. P. B.Katehi , IEEE Trans. Microwave Theory Tech. **44**, 555 (1996).

[26] M. Tentzeris, J. Harvey, IEEE Microwave Guided Wave Lett. **9**, 96 (1999).

[27] M. Toupikov, G. Pan, IEEE Trans. Microwave Theory and Techniques **48**, 500 (2000).

[28] R.Ramesh, M.Madheswaran, K.Kannan, Journal of Optoelectronics And Advanced Materials 12, 5 (2010)

[29] F. P. Bolin, L. E. Preuss, R. C. Taylor, R. J. Ference, Appl. Opt. **28**, 2297 (1989).

---

*Corresponding author: ramesh24.dr@gmail.com